nature communications

Article

https://doi.org/10.1038/s41467-026-76012-6

Ultrafast bimolecular reaction catalysis via engineered nuclear quantum effects in helium nanodroplets

Received: 28 November 2025

Accepted: 17 July 2026

Published online: 30 July 2026

Check for updates

Jiaxuan Chen[1,9], Leshi Zhao[2,9], Hao Huang[2,9], Zhengjun Ye[1], Yue Hu[1], Menghang Shi[1], Xinglei Long[1], Cristina Sanz-Sanz[3], Octavio Roncero[4], Ling Liu[2], Xinzheng Li[2], Hongcheng Ni[1,5] ✉, Zheng Li[6,7] ✉, Wenbin Zhang[1,5] ✉ & Jian Wu[1,5,8] ✉

Nuclear quantum effects (NQEs) fundamentally alter chemical reactivities, particularly those occurring at low temperatures or involving light nuclei. Yet, directly resolving how NQEs influence the ultrafast dynamics of bond formation remains a central challenge. Here we report the time-resolved observation of NQEs catalyzing a light-induced bimolecular reaction within a quantum-phase environment. Using femtosecond pump-probe spectroscopy on H_2-H_2 and D_2-D_2 dimers confined in helium nanodroplets at 0.37 K, we find that the low-temperature conditions engineered by the host environment drive a pronounced acceleration of reaction dynamics. The formation of H_3^+ is accelerated to 59 ± 10 fs in the droplet compared to 152 ± 17 fs in the gas phase. This catalytic effect is strongly isotope-dependent, with the heavier D_3^+ exhibiting only a slight reduction in formation time from 153 ± 8 fs to 111 ± 9 fs. Molecular dynamics simulations reveal that the acceleration is catalyzed by pronounced NQEs under cryogenic confinement, with lighter hydrogen isotopes exhibiting greater quantum delocalization and consequently faster reaction rates. These findings provide a time-resolved perspective on quantum effects in ultracold chemistry, demonstrating how the unique environment of nano-cryo-reactors can harness temperature-driven NQEs to steer the ultrafast dynamics of chemical reactions.

At low temperatures, molecular chemical reactions often exhibit counterintuitive behavior, such as proceeding with high efficiency despite minimal thermal energy. This phenomenon is driven by enhanced nuclear quantum effects (NQEs)[1–3], where the wave-like nature of nuclei enables quantum tunneling and wavefunction delocalization[4,5]. NQEs have been found to play critical roles in biology, chemistry, and material science, affecting the proton hopping within zeolite catalysis[6], the genetic stability of DNA[7,8], and the properties of

[1]State Key Laboratory of Precision Spectroscopy, East China Normal University, Shanghai, China. [2]State Key Laboratory for Mesoscopic Physics and Frontiers Science Center for Nano-Optoelectronics, School of Physics, Peking University, Beijing, China. [3]Departamento de Química Física Aplicada, Módulo 14, Facultad de Ciencias, Universidad Autónoma de Madrid, Madrid, Spain. [4]Instituto de Física Fundamental, CSIC, Serrano 123, Madrid, Spain. [5]Collaborative Innovation Center of Extreme Optics, Shanxi University, Taiyuan, Shanxi, China. [6]School of Science and Hubei Key Laboratory of Optical Information and Pattern Recognition, Wuhan Institute of Technology, Wuhan, China. [7]Wuhan National Laboratory for Optoelectronics and School of Physics, Huazhong University of Science and Technology, Wuhan, China. [8]Chongqing Key Laboratory of Precision Optics, Chongqing Institute of East China Normal University, Chongqing, China. [9]These authors contributed equally: Jiaxuan Chen, Leshi Zhao, Hao Huang. ✉e-mail: hcni@lps.ecnu.edu.cn; zhengli@wit.edu.cn; wbzhang@lps.ecnu.edu.cn; jwu@phy.ecnu.edu.cn

superconductor materials[9]. Driven by this broad importance, the field of cold molecules has emerged as a powerful platform for studying these quantum-dominated reactions. By precisely controlling internal degrees of freedom of the reactants[10], researchers can investigate reaction dynamics and mechanisms in unprecedented details[11,12]. Techniques like velocity map imaging, combined with ultracold molecule preparation, have further enabled the study of unstable intermediate complex and product state distributions[13]. Yet, the time-resolved dynamics of cold molecular reactions, particularly how NQEs influence the femtosecond timescales of bond formation, remain poorly understood, as traditional beam and spectroscopy measurements lack the temporal resolution to capture such ultrafast processes.

The H_3^+ ion, formed through the bimolecular reaction $H_2^+ + H_2 \rightarrow H_3^+ + H$[14], plays a pivotal role in interstellar chemistry, initiating chemical reactions that lead to water and organic molecules formation[15]. This reaction is particularly relevant in cold environments like the interstellar medium and planetary atmospheres, where temperatures can drop to a few Kelvins (K) or sub-K, enhancing NQEs. Laboratory studies using laser techniques have clarified H_3^+ formation mechanisms in organic systems, revealing a sequence of bond-breaking and bond-making events[16,17]. Recent research has also demonstrated environmental catalysis in H_3^+ generation from H_2O molecules on nanoparticle surfaces[18], and explored D_3^+ formation dynamics from D_2-D_2 dimers in the gas phase[19,20]. However, the influences of relevant cold environments on ultrafast dynamics of these reactions, especially where NQEs are pronounced, remain largely unexplored. Investigating these reaction dynamics under controlled cold conditions is crucial for accurately modeling the chemistry of astrophysical environments.

Helium nanodroplets (He_N) serve as a unique platform for studying cold chemical reactions at ultralow temperatures of $T = 0.37$ K, simulating the conditions relevant to the interstellar medium and planetary atmospheres. These superfluid droplets act as nano-cryo-reactors that can capture and aggregate atoms and molecules as dopants. Due to the inert and superfluid environment, the internal degrees of freedom of embedded molecules are efficiently cooled to 0.37 K through He atom evaporation, yet their rovibronic structures experience minimal perturbation. This unique setting enables the study of fundamental chemical interactions that are often obscured in bulk phases or warmer gas-phase experiments, as first demonstrated in the reaction $Ba + N_2O \rightarrow BaO^* + N_2$[21] and since explored in other systems[22–24]. Crucially, at this cryogenic temperature, molecules exhibit significant quantum behavior, characterized by an increased de Broglie wavelength $\lambda_{dB} = h/\sqrt{2\pi m k_B T}$ and spatially extended molecular wave functions. This effect is especially pronounced for molecules with lighter atoms. The He_N environment, therefore, serves as an ideal laboratory for enhancing and isolating NQEs.

In this article, we investigated the ultrafast formation dynamics of H_3^+ and D_3^+ in light-induced bimolecular reaction of H_2-H_2 and D_2-D_2 dimers within He_N, and made a comparison to those in the gas phase. By performing pump-probe experiments in a reaction microscope, we measure the time-dependent yields of H_3^+ and D_3^+, revealing their formation timescales. Interestingly, we observe that H_3^+ forms significantly faster in helium droplet than that in gas phase (~59 ± 10 fs vs. ~152 ± 17 fs), whereas the acceleration for D_3^+ is less pronounced (~111 ± 9 fs vs. ~153 ± 8 fs). Our path integral and quasi-classical molecular dynamics simulations attribute this difference to enhanced NQEs at lower temperatures, with lighter atoms experiencing greater quantum delocalization of their nuclear wavefunctions, thereby accelerating the reaction.

Results

Experimental identification of H_3^+ and D_3^+ formation channels

The experimental measurements were performed in a reaction microscope (COLTRIMS) setup (see Fig. 1a)[25]. Dimers of H_2 or D_2 were studied both inside He_N and in the gas phase. The in-droplet dimers were formed by doping a continuous He_N beam, generated via supersonic expansion, with H_2 or D_2 gas. Gas-phase dimers were created by the supersonic expansion of pure H_2 or D_2, achieving a translational temperature of ~30 K[26]. A pump-probe configuration with two linearly polarized femtosecond laser pulses (~38 fs, 790 nm, 10 kHz) was used to interact either with the droplet beam or the molecular beam. The time-of-flight (TOF) spectra and impact position of laser-created ionic fragments were recorded using a time and position sensitive microchannel plate detector, enabling the identification of distinct ionization processes. More experimental details are provided in the "Methods" section.

Figures 1b–e present the measured ion yield distributions for various jet scenarios, plotted as a function of the TOF and the impact position along the y-axis at the detector. For the H_2-doped droplet beam [Fig. 1b], the predominant signals of H_2^+ and H^+ are produced from the laser-induced dissociative ionization of gas-phase free H_2 molecules, originating from the doping cell leakage and residual background gas. Within the droplets, photoionization of embedded H_2 molecules mainly produces H^+ and H_2^+ ions via dissociative ionization or H_3^+ via an exoergic bimolecular reaction. These energetic H^+, H_2^+ or H_3^+ ions from the droplet interior are either detected directly with mass-to-change ratios (m/q) of 1, 2 or 3, respectively, or registered as spectroscopic byproducts of He_nH^+, $He_nH_2^+$, $He_nH_3^+$ (n = 1, 2, 3, ...) with relatively lower yields (see Supplementary Fig. S1 for details), formed through binding with different numbers of He atom as they exit the droplet. Similarly, in the D_2-doped scenario [Fig. 1c], the dominant D_2^+ and D^+ signals, resulting from gas-phase D_2 molecule ionization, are also clearly distinguishable from the D_3^+, $He_nD_2^+$, $He_nD_3^+$ (n = 1, 2, 3, ...) fragments generated from in-droplet D_2-D_2 dimer. We note that in the D_2-doped droplet data, although there is inherent TOFs overlap between the TOFs of HeD^+ and D_3^+ due to the degeneracy in their mass-to-charge ratio (m/q = 6). However, we can unambiguously isolate and identify these ion fragments by their distinct kinetic energy (E_{kin}) spectra[27], where the energetic HeD^+ fragments are assigned to $E_{kin} > 0.08$ eV, and the in-droplet D_3^+ ions are filtered for $E_{kin} < 0.08$ eV. Notably, the formation of gas-phase H_2-H_2 and D_2-D_2 dimers from residual H_2 or D_2 gas leaking into the interaction chamber is negligible due to the low pressure in the doping chamber. This is corroborated by the absence of H_3^+, $He_nH_2^+$, $He_nH_3^+$ and D_3^+, $He_nD_2^+$, $He_nD_3^+$ signals when the droplet source is blocked from the doping region. In contrast, when employing supersonic H_2 or D_2 gas jet, as shown in Fig. 1d, e, clearly discernible H_3^+ and D_3^+ signals are observed, arising from the light-induced bimolecular reaction starting from gas-phase H_2-H_2 and D_2-D_2 dimers, respectively.

Time-resolved H_3^+ and D_3^+ formation dynamics

Building on the evidence of H_3^+ and D_3^+ formation in both droplets and gas-phase environments, we proceed to investigate their ultrafast formation dynamics utilizing pump-probe spectroscopy. Recent studies have clarified the mechanisms of H_3^+ formation from gas-phase H_2-H_2 dimers[19,20]. The process initiates when the pump pulse ionizes the dimer via multiphoton ionization, producing $H_2 - H_2^+$ in its cation state, serving as the reaction's starting point. Subsequently, the H_2^+ ion interacts with the neighboring H_2 molecule, triggering atomic rearrangements that bond three hydrogen atoms into H_3^+, while the remaining hydrogen atom departs. Once this atom moves for a sufficient distance, the H_3^+ ion is stably formed. If the probe pulse arrives during this sequence, it may perturb the intermediate $H_2 - H_2^+$ cation, potentially through dissociation or secondary ionization. This ultrafast disruptive probing mechanism, detailed in[28], disrupting H_3^+ formation. By measuring the time-dependent yield of H_3^+ as a function of pump-probe delay, one can uncover the ultrafast dynamics of this bimolecular reaction.

https://doi.org/10.1038/s41467-026-76012-6

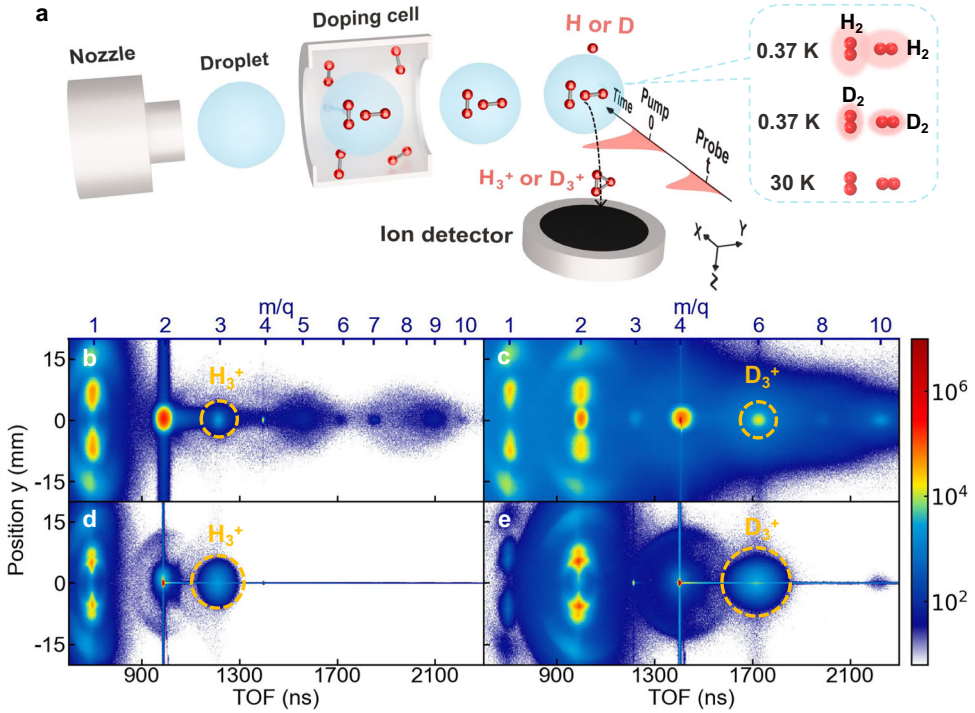

Fig. 1 | Experimental scheme. a Schematic diagram of the experimental setup. Gas-phase H_2 or D_2 dimers are produced by the supersonic expansion of the H_2 or D_2 gas through the nozzle. The square inset illustrates the initial dimer states: H_2 nuclei show broad spatial delocalization in 0.37 K helium nanodroplets, whereas D_2 nuclei show only weak delocalization. No delocalization is observed for either species in the 30 K gas phase. **b**–**e** Measured ion yield distributions as a function of the TOF and y position of impact for various jet scenarios: **b** H_2-doped droplets jet, **c** D_2-doped droplets jet, **d** supersonic jet of H_2 gas, and **e** supersonic jet of D_2 gas. The accompanying H^+ and H_2^+ signals in (**c**, **e**) primarily result from photoionization of free H_2 molecules in the residual background. The orange dashed circles serve as visual guides to highlight the approximate positions of the relevant H_3^+ and D_3^+ signals, rather than the exact integration boundaries.

Figure 2a displays the H_3^+ ion yields produced from gas-phase H_2-H_2 dimers as a function of time delay. As shown in the inset, when the probe pulse precedes the pump pulse at negative time delays, the H_3^+ yield remains constant. This stability arises because the weak probe pulse alone cannot generate $H_2 - H_2^+$ cations and, arriving first, does not interfere with the reaction initiated by the pump pulse. When the probe pulse arrives after the pump pulse, the H_3^+ yield initially drops to a minimum, then rises exponentially before reaching a plateau. At short positive delay, the probe pulse disrupts the intermediate $H_2 - H_2^+$ cation before H_3^+ can form, causing a depletion in the H_3^+ yield. As the delay increases, this disruption diminishes, allowing the yield to recover. Consequently, the recovery timescale reflects the H_3^+ formation time. By fitting the recovery curve in Fig. 2a with a mono-exponential function of $y = A\exp(-t/\tau) + y_0$, where A is the amplitude, τ is the time constant and y_0 is the offset, we determine the formation time τ for H_3^+ to be 152 ± 17 fs at a 95% confidence level. Notably, as depicted in Fig. 2c, the formation time for gas-phase D_3^+, $\tau = 153 \pm 8$ fs, is nearly identical to that of gas-phase H_3^+. We note that our measured gas-phase D_3^+ formation time is highly consistent with the ~139 fs timescale reported by Zhou et al.[19], while differing from the ~330 fs timescale reported in a parallel study by Mi et al.[20]. This discrepancy likely originates from differences in the supersonic expansion parameters, which govern the initial thermodynamic temperature and rovibrational distribution of the neutral dimers, as well as different theoretical criteria used to define the spatial separation at which the fragments are considered stably formed. Our measurement of nearly identical gas-phase formation times for both H_3^+ and D_3^+ provides robust internal confirmation of this ~150 fs timescale, demonstrating that the dynamics at ~30 K are governed by classical motion on a steep, barrierless potential, rendering the timescale largely insensitive to isotopic mass.

Interestingly, however, the underlying reaction mechanism fundamentally shifts when the bimolecular reactions occur within the cold He_N environment. Figure 2b, d show the time-dependent yields of H_3^+ and D_3^+ ions from in-droplet H_2-H_2 and D_2-D_2 dimers, respectively. The formation time constant for H_3^+ in He_N is extracted to be $\tau = 59 \pm 10$ fs, which is significantly shorter than that observed in the gas phase. In contrast, for in-droplet D_3^+, the time constant is $\tau = 111 \pm 9$ fs, indicating a less pronounced acceleration, with only ~42 fs reduction compared to the gas-phase value. These distinct time constants suggest that the cold conditions of He_N disproportionately speed up the formation of H_3^+ over D_3^+, pointing to the influence of quantum mechanical effects tied to the mass of the reactants.

Acceleration of reaction dynamics by NQEs

This striking difference arises primarily from the cold environment of the He_N, where in-droplet molecules are cooled to 0.37 K, compared to approximately 30 K in the gas phase achieved via supersonic expansion. While this direct experimental comparison inherently couples the effects of the ultracold temperature and the physical confinement of the droplet, our complementary theoretical simulations (discussed below) successfully disentangle them, demonstrating that the 0.37 K temperature is the dominant driver of the acceleration. At this low temperature, the extent of the wavefunction of the lightest H_2 molecules expands significantly, resulting in a broader spatial distribution of H_2. This leads to a notable delocalization of each H_2 molecule within the droplet, enhancing the overlap of wavefunctions between the two H_2 molecules involved in the bimolecular reaction. Such increased overlap can effectively increase the interaction cross-section and significantly change the formation process, thereby accelerating the formation of H_3^+. In contrast, for D_2 molecules, which have a larger mass, the spatial extent of the molecule's wavefunction is narrower compared to H_2, leading to a higher degree of localization within the

https://doi.org/10.1038/s41467-026-76012-6

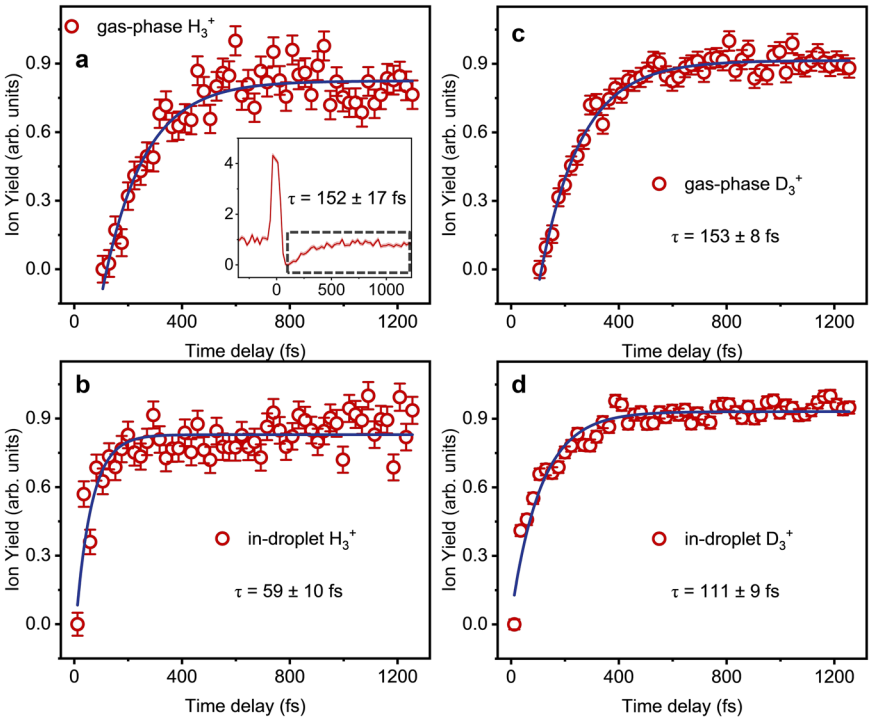

Fig. 2 | Measured time-dependent normalized yields of H_3^+ and D_3^+ ions for different jet scenarios. a gas-phase H_3^+, **b** in-droplet H_3^+, **c** gas-phase D_3^+, and **d** in-droplet D_3^+. Experimental data (red hollow dots) are shown with exponential fits (blue solid lines). Normalization is performed such that the minimum value of the yield is 0 and the maximum value of the yield is 1. The data are presented as normalized yields ± standard deviation. The inset of **a** shows the measured full pump-probe delay trace of gas-phase H_3^+ yield scanning from −300 fs to 1280 fs, and the corresponding full traces for (**b**–**d**) can be found in the Supplementary Fig. S2.

0.37 K droplet. As a result, the quantum effects are less pronounced for D_2, and the formation process of D_3^+ in He_N exhibits less deviation from that in the gas phase, resulting in only a slight acceleration of the reaction. This pronounced isotopic asymmetry effectively rules out a purely classical 'cage effect', where droplet environment physically restricts the fragment excursion length, as the primary acceleration mechanism, since classical spatial confinement would accelerate both isotopes similarly. Furthermore, the observed acceleration cannot be attributed to structural changes in the initial dimers, as the weak van der Waals interaction with the superfluid helium solvent is insufficient to alter their classical equilibrium geometry. These observations highlight how the ultracold conditions in He_N amplify NQEs, particularly for lighter molecules like H_2, profoundly influencing the dynamics of bimolecular reactions.

Molecular dynamics simulations

To elucidate the isotope-specific acceleration for the ultrafast bimolecular reaction dynamics of H_3^+ and D_3^+ formation at low temperatures, we first performed the ring-polymer molecular dynamics (RPMD) simulations[29]. According to the de Broglie relation[30], the quantum wave-packet is more significant for lighter nuclear masses or lower temperatures, making classical dynamics an insufficient approximation in these regimes[31–34]. The RPMD[29], based on the Feynman path integral principle[35], provides an approximate dynamical framework for incorporating NQEs[36–38], including contributions from both the initial quantum distribution and the subsequent nuclear dynamics. In RPMD, each nucleus is mapped to a classical ring polymer consisting of n beads, connected end-to-end by harmonic springs. Each bead has the same mass as the nucleus, with the angular frequency of harmonic potential $\omega_n = nk_BT/\hbar$, where n is the number of beads, k_B is the Boltzmann constant, T is the temperature, and $\hbar$ is the reduced Planck constant. At low temperatures, the springs become very weak and allow significant bead dispersion that mimics the delocalization of nuclear wavefunctions and thus highlights NQEs. More details of the RPMD simulations can be found in the "**Methods**" section.

The RPMD simulation results, presented in Fig. 3a, b, reveal distinct differences in the formation dynamics of H_3^+ and D_3^+ under varying temperature conditions. At 30 K, the most probable formation times extracted from the fitting curves are 144 ± 8 fs for H_3^+ and 147 ± 18 fs for D_3^+, respectively. This indicates that NQEs have a minimal impact on formation rates at this temperature, despite the differing masses of H and D nuclei. At 0.37 K, however, the formation times decrease significantly to 60 ± 5 fs for H_3^+ and 84 ± 4 fs for D_3^+, reflecting a marked acceleration compared to 30 K. This enhanced reaction rate at the lower temperature results from stronger NQEs, which enhance the delocalization of nuclear wavefunctions, thereby facilitating faster reaction dynamics. The lighter hydrogen nucleus amplifies this effect, leading to a more pronounced acceleration for H_3^+ compared to D_3^+. These findings underscore the important role of NQEs at low temperatures in driving the rapid formation of H_3^+ and D_3^+, with a greater influence on the lighter hydrogen system.

To further disentangle the relative contribution of NQEs from the initial-state distribution versus those from quantum propagation, we also performed dimension-reduced quasi-classical trajectory (DR-QCT) simulations. This approach captures the essential reaction dynamics[19,20] but, crucially, neglects quantum effects during the dynamical propagation of the trajectory (see "**Methods**" for simulation details). For both H_2-H_2 and D_2-D_2 dimers, reactions were initiated from the most stable, T-shaped configuration. We tracked two key coordinates: the distance from the undissociated molecule to the atomic cation, and the bond length of the dissociating molecule. To incorporate NQEs arising from the initial-state distribution, the starting conditions for each trajectory were sampled from the quantum probability distribution of the ground-state wavefunction in the two-dimensional coordinate space. The trajectories were then

https://doi.org/10.1038/s41467-026-76012-6

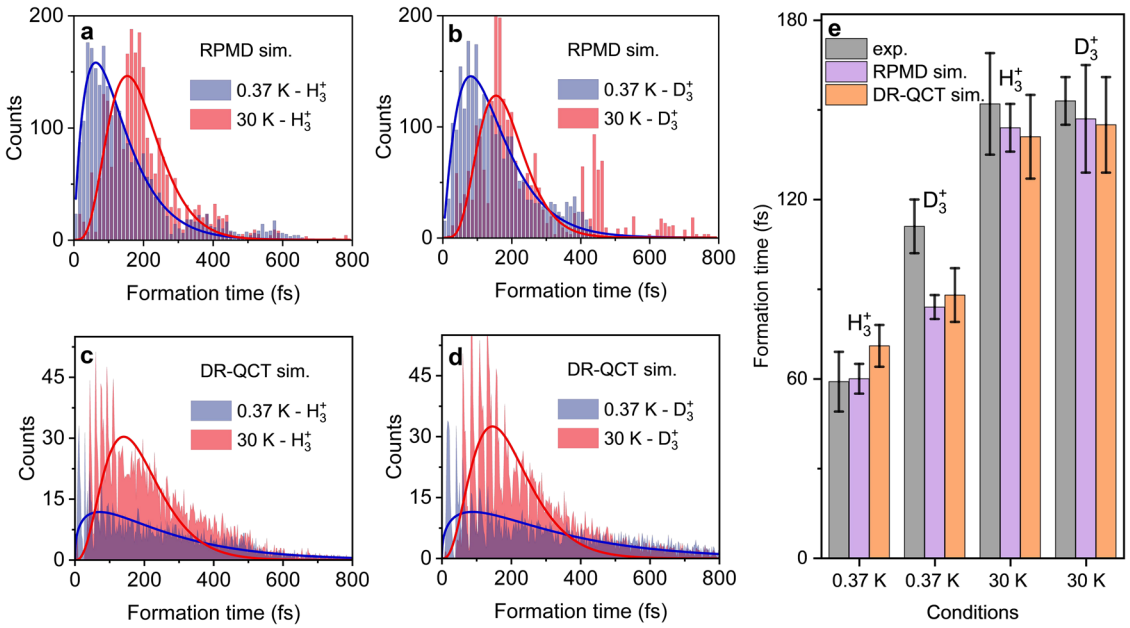

Fig. 3 | Simulated H_3^+ and D_3^+ formation time under different conditions. Panels **a**–**d** show histograms of formation times for **a**, **c** H_3^+ and **b**, **d** D_3^+ at 30 K (gas-phase) and 0.37 K (in-droplet). The results are obtained from two different theoretical models: **a**, **b** ring-polymer molecular dynamics (RPMD) and **c**, **d** dimension-reduced quasi-classical trajectory (DR-QCT). Panel **e** compares the average formation times from both simulations to experimental measurements for both ions at both temperatures.

propagated classically on the corresponding potential energy surface.

The resulting formation times from the DR-QCT simulations are shown as histograms in Fig. 3c, d, where the peak position of the fitted curve in each panel represents the most probable formation time. At 30 K in the gas phase, our simulations yield formation times of 141 ± 14 fs for H_3^+ and 145 ± 16 fs for D_3^+, showing close agreement with the experimental results. In contrast, the dynamics at 0.37 K within the He_N are significantly different. The cryogenic environment enhances NQEs, leading to pronounced quantum delocalization of the nuclei, which exhibits a broad spatial distribution within the confined potential of helium droplets[39]. This delocalization allows a substantial statistical fraction of dimers to sample much shorter internuclear distances, providing a distribution of initial conditions that directly catalyze the reaction. As a result, the most probable formation times shorten markedly to 71 ± 7 fs for H_3^+ and 88 ± 9 fs for D_3^+. This provides direct evidence that enhanced NQEs in the initial state, amplified by the cryogenic droplet environment, significantly accelerate the formation of trihydrogen cations.

A direct comparison of the average formation times from the RPMD and DR-QCT simulations against the experimental measurements is presented in Fig. 3e. Both simulation methods successfully predict a pronounced acceleration in the formation rates at 0.37 K and show that this acceleration is more pronounced for H_3^+ than for D_3^+. Crucially, the DR-QCT model, which only considers NQEs in the initial state, already captures the overall trend and provides results that align well with experimental data. This provides direct evidence that enhanced NQEs in the initial state are the primary driver of the reaction at ultralow temperatures. In comparison, the RPMD model offers a more comprehensive and physically accurate picture by also incorporating NQEs during the reaction propagation. This supplementary quantum effect is reflected in H_3^+ formation at 0.37 K, where RPMD predicts a faster formation time (60 fs) than DR-QCT (71 fs), bringing the result closer to the experimental value of 59 fs. This suggests that quantum phenomena during the dynamical evolution slightly accelerate the reaction. The strong concordance between these two distinct theoretical models lends high confidence to the central conclusion that the NQEs in both initial state and dynamics evolution are the critical factor governing these ultrafast, low-temperature reactions.

Influence of the helium solvent environment

Having established the primary role of NQEs in accelerating the H_3^+ and D_3^+ formation reaction, we also explore whether the He_N environment itself influences this dynamics by investigating the role of surrounding helium atoms. In the nanodroplet, numerous helium atoms encircle the $(H_2\text{-}H_2)^+$ or $(D_2\text{-}D_2)^+$ complexes, where electrostatic interactions could polarize nearby helium atoms and affect the dynamical evolution of these ions. We use the self-consistent continuum solvation model[40] to quantify the impact of the helium surroundings on the formation of H_3^+ and D_3^+ (see "Methods" for simulation details).

Figure 4 shows the averaged trajectories, comparing the formation of H_3^+ and D_3^+ with and without the influence of the helium droplet's polarization effect. Based on the defined criteria for atomic approaching and departing distances (see inset Fig. 4a), we calculated the average formation times. Note that since the significant NQEs at 0.37 K are not incorporated in these specific simulated trajectories, the obtained baseline formation times are close to the gas-phase values rather than the accelerated RPMD results shown in Fig. 3. For H_3^+, the average formation time was 122 fs without the helium environment and 135 fs with it, revealing a modest slowing effect that increases the formation time by approximately 13 fs (Fig. 4a). The retardation effect was more pronounced for D_3^+, where the average formation time increased from 132 fs to 163 fs, with a delay of 31 fs (Fig. 4b). This greater hindering effect for D_3^+ can be attributed to a separate isotope effect related to the solvent interaction. As D nuclei are more massive than H nuclei, their nuclear wave function is more spatially localized. Consequently, the polar interaction between D atoms and the polarized helium environment is stronger. This enhanced attraction, depicted in the inset of Fig. 4b, hinders the final formation of D_3^+ more effectively than it does for H_3^+.

Thus, the helium nanodroplet environment plays a dual role in shaping the reaction. Its evaporative cooling provides the ultracold 0.37 K thermodynamic conditions that drastically accelerate the reaction via enhanced NQEs. Conversely, its physical presence as a polarizable solvent introduces a minor, opposing retardation effect

https://doi.org/10.1038/s41467-026-76012-6

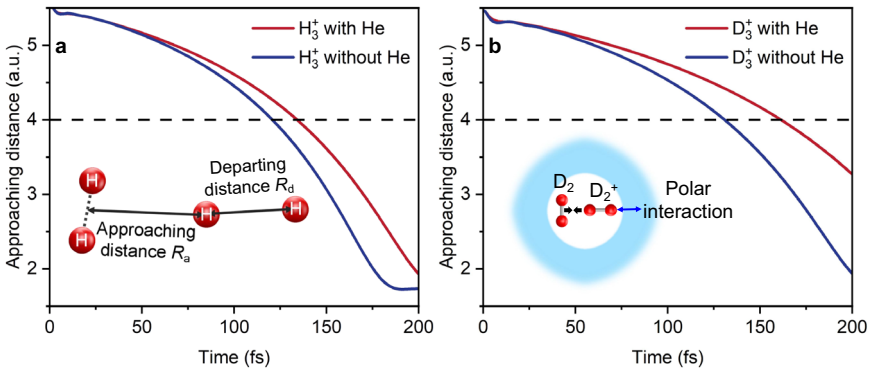

Fig. 4 | Retardation effect of helium surroundings on the H_3^+ and D_3^+ formation. **a**, **b** Typical trajectories showing approaching distance (R_a) toward the formation of **a,** H_3^+ and **b,** D_3^+ with and without the influence of the helium droplet's polarization effect. The inset in **a** illustrates the definition of approaching (R_a) and departing distances (R_d) during the bimolecular reaction dynamics. The critical value of R_a for judging that H_3^+ and D_3^+ are formed is indicated by the horizontal dashed lines at $R_a = 4$ a.u. The inset in **b** depicts the polarizable interaction between the dimer in He_N and the nearby polarized helium hindering D_3^+ formation. The white circular area indicates the solute cavity containing the in-droplet D_2 dimer. The light blue area outside the solute cavity corresponds to the solvent environment. The black arrows indicate that the three D atoms approach each other following ionization to form D_3^+, whereas the blue arrow represents the polar interaction that hinders D_3^+ formation.

that slightly slows the nuclear rearrangement, particularly for the heavier deuterium. It is crucial to note that this solvent-induced retardation is much smaller in magnitude compared to the dominant acceleration caused by the low-temperature-driven nuclear quantum delocalization, which ultimately defines the overall reaction dynamics. By comprehensively considering these solvent-induced retardation (a delay of +13 fs vs. +31 fs) and our RPMD results (60 fs vs. 84 fs), we achieve a complete theoretical picture that well reproduces the experimental kinetic isotope effect (KIE) observed in droplets (59 fs vs. 111 fs), demonstrating that both NQEs and solvent interactions are required to fully explain the in-droplet dynamics.

Discussion

In conclusion, we have elucidated the important role of ultralow-temperature-driven NQEs, enabled by the unique environment of He_N, in accelerating the ultrafast reaction dynamics of H_2-H_2 and D_2-D_2 dimers. By performing femtosecond pump-probe experiments, we measured the formation dynamics of H_3^+ and D_3^+ in both He_N and the gas phase. The in-droplet H_2-H_2 dimer enhanced delocalization of their nuclear wavefunctions, leading to a substantial reduction in reaction time compared to the gas phase. Moreover, the heavier D nuclei result in less pronounced NQEs, yielding only modest acceleration for D_3^+ formation. Although these theoretical frameworks inherently rely on approximations, such as the continuum treatment of the superfluid helium and the explicit decoupling of initial-state and dynamical effects, the path integral and dimension-reduced quasi-classical molecular dynamics simulations successfully reproduce the qualitative kinetic isotope trends. While the precise quantitative agreement with the experiment should be interpreted cautiously, the simulations provide robust mechanistic evidence, unveiling the critical impact of NQEs in driving the ultrafast reaction dynamics. Importantly, we expect these environmentally engineered quantum accelerations to be most pronounced for reactions involving extremely light nuclei and proceeding along the barrier-less potential energy surfaces, where initial-state spatial delocalization can maximally short-circuit classical reaction pathways. Our findings not only advance the understanding of NQEs in chemical reactions by providing a time-resolved perspective on how quantum mechanics governs the ultrafast formation dynamics in bimolecular reactions but also open numerous possibilities of exploring the detailed role of quantum behavior in ultracold chemical reactions through the unique platform offered by He_N.

Methods

Experimental details

The experimental setup is schematically depicted in Fig. 1a. The in-droplet and gas-phase H_2-H_2, D_2-D_2 dimers were produced using distinct methods. A continuous He_N beam was generated through the supersonic expansion of high-purity ^{4}He gas (>99.9999%) from a 20-bar stagnation pressure through a 5-μm-diameter nozzle pre-cooled to (18 K). This process yielded droplets with a mean size of approximately 2 nm, containing on average ~1000 He atoms per droplet[41]. The He_N beam then traversed a 4-cm-long pickup cell containing either H_2 or D_2 gas. The pressure of the flowing H_2 or D_2 within this cell was carefully regulated to 8×10^{-6} mbar during the measurements. Based on the Poisson distribution governing the doping process, this ensures an average doping of two molecules (H_2 or D_2) per droplet. The low-temperature environment of the He_N facilitated the aggregation of the doped molecules into H_2-H_2 or D_2-D_2 dimers. For comparison, gas-phase H_2-H_2 or D_2-D_2 dimers were produced by supersonically expanding pure H_2 or D_2 gas through the same nozzle setup. A driving pressure of 2 bar was used, resulting in a translational beam temperature of approximately 30 K[26]. The dimer targets, either in the droplet or gas phase, were interrogated using two linearly polarized femtosecond laser pulses (~ 38 fs, 790 nm, 10 kHz) in a pump-probe arrangement. These pulses were focused onto the beam inside the COLTRIMS apparatus by a concave silver mirror ($f = 7.5$ cm). The in situ peak intensity of the linearly polarized laser pulses in the interaction region was calibrated by measuring the intensity-dependent TOF spectra of protons produced from the dissociative ionization of H_2. By comparing these measurements with established reference data[42], the laser peak intensities were determined with an estimated uncertainty of ± 10%. For the measurements involving helium droplets, the peak intensities for the pump and probe pulses were approximately ~1.7×10^{14} W/cm^2 and ~1.2×10^{14} W/cm^2, respectively. To avoid detector saturation due to the higher target density in the pure gas-phase experiments, the laser intensities were reduced to ~1.1×10^{14} W/cm^2 for the pump pulse and ~0.5×10^{14} W/cm^2 for the probe pulse. We note that because the pump and probe pulses act purely to initiate and subsequently disrupt the reaction, the actual nuclear rearrangement evolves field-free; thus, the extracted formation times remain independent of these specific variations in the applied laser intensity.

RPMD simulation details

In RPMD simulations, the Hamiltonian of n beads composed ring polymers of N-nuclei molecule is[29]

$$H_n(\vec{q},\vec{p},t)=\sum_{i=1}^{n}\sum_{j=1}^{N}\left(\frac{|\vec{p}_{i;j}|^2}{2m_j}+\frac{1}{2}m_j\omega_n^2|\vec{q}_{i;j}-\vec{q}_{i-1;j}|^2+V_i(\vec{q}_{i;1},\ldots,\vec{q}_{i;N},t)\right), \quad (1)$$

where $\vec{q}$ and $\vec{p}$ represent the collective position and momentum of the n beads composed ring polymers of N-nuclei respectively, $\vec{q}_{i;j}$ and $\vec{p}_{i;j}$ represent the position and momentum of the j-th nucleus in the i-th bead respectively, m_j is the mass of the mapped j-th nucleus, $V_i(\vec{q}_{i;1},\ldots,\vec{q}_{i;N},t)$ is the average field generated by the many-body electron wave function of the i-th bead, that is, the adiabatic potential energy surface where the i-th bead is located, and it can be calculated using the first principle method. The RPMD method provides the dynamic description of a quantum system by calculating the classical dynamic evolution of ring polymers[29]. From the perspective of quantum mechanics, by considering the isomorphic relationship between classical systems and quantum systems, the possible dynamical states of nuclei are given by time-dependent evolving beads[43]. By sampling the classical trajectory of beads, we can obtain the dynamical evolution of the nuclear wave function.

For the RPMD simulations of the dynamical evolution of $(H_2\text{-}H_2)^+$ and $(D_2\text{-}D_2)^+$ at 0.37 K (in-droplet) and 30 K (gas-phase), we employed the i-PI 3.0 software package[44] to perform both the initial state sampling and the subsequent quantum dynamics calculations. To ensure an accurate description of the intermolecular interactions and reactive regions, we utilized high-precision global full-dimensional potential energy surfaces (PESs). Specifically, the neutral equilibration of H_2-H_2 and D_2-D_2 was performed on a Permutation Invariant Polynomial Neural Network (PIP-NN) PES[45], while the subsequent cationic reactive dynamics adopted an accurate MRCI-level PES[46,47] to properly capture the strong electron correlation during bond formation.

Initially, we conducted full-dimensional path integral simulations for the neutral systems. To capture the pronounced nuclear quantum delocalization at extreme low temperatures, we implemented the high-order Suzuki-Chin (SC) path integral scheme[48] using 512 beads. A stringent integration time step of 0.1 fs was used to guarantee numerical stability and energy conservation, incorporating a PILE thermostat to achieve the steady state. Furthermore, for the D_2-D_2 system, identical particle exchange effects were explicitly included by activating the bosonic path integral algorithm[49] within i-PI. The distinguishable particle assumption was retained for the H_2-H_2 system due to the limitations associated with the fermion sign problem[50]. This treatment is additionally justified by our simulations for the $(D_2\text{-}D_2)^+$ system, which demonstrated that identical particle exchange effects have a negligible influence on the reaction timescales for this specific ultrafast process.

Following the equilibration of the neutral systems, the sampled configurations were used as initial conditions to simulate the dynamical evolution of the charged $(H_2\text{-}H_2)^+$ and $(D_2\text{-}D_2)^+$ complexes via RPMD within the microcanonical (NVE) ensemble by switching the underlying interactions to the respective cationic MRCI-level PES[46,47]. For the cationic dynamics, standard RPMD propagation replaces the high-order SC scheme, lifting its stringent numerical constraints and allowing us to safely relax the integration time step to 0.5 fs. This step size remains significantly smaller than the fastest H-H or D-D vibrational period, seamlessly maintaining physical accuracy and algorithmic stability while avoiding prohibitive computational costs. To obtain statistically converged reaction timescales, we generated a large ensemble of trajectories. Specifically, we collected 2560 reactive trajectories for both $(H_2\text{-}H_2)^+$ and $(D_2\text{-}D_2)^+$ at 0.37 K. At 30 K, 2560 and 2457 reactive trajectories were analyzed for $(H_2\text{-}H_2)^+$ and $(D_2\text{-}D_2)^+$, respectively, excluding a small number of non-reactive events. Finally, we analyzed the trajectory of each bead to determine the formation dynamics[19,20]. The formation of H_3^+ and D_3^+ is registered when the approaching distance R_a contracts below 4 a.u. and the departing distance R_d simultaneously stretches beyond 5 a.u. This criterion is grounded in the observation that the PES becomes exceedingly flat within this region, indicating the completion of the reaction and the stabilization of the products.[19]. The trajectories leading to the successful formation of H_3^+ and D_3^+ were collected to construct the temporal yield distributions. To systematically extract the macroscopic reaction timescales, these distributions were fitted using a Gamma distribution $f(t) = \alpha t^{k-1}e^{-t/\tau}$, where α is an overall scaling factor, k is a shape parameter, and τ is a scale parameter. The peak positions of the fitted Gamma distribution curves were subsequently extracted and assigned as the most probable time for the formation of H_3^+ and D_3^+.

DR-QCT simulation details

The DR-QCT simulations combine quantum-mechanical sampling of initial reactant conditions with subsequent purely classical trajectory propagation. In DR-QCT simulations, the initial positions for the reaction trajectories are sampled from the spatial distribution of the initial quantum state of the neutral dimer. For the gas-phase dimer at 30 K, this initial state is prepared as a Boltzmann-weighted superposition of the vibrational ground and excited states, obtained via imaginary-time propagation. To model the dimer in a droplet at 0.37 K, we obtain the centroid distance of the dimer $|R_a + R_d|/2$ by simultaneously sampling the centroid positions of two hydrogen molecules in three dimensions according to the normalized radial probability density distribution within He_N[39]. The initial bond length of the dissociating molecule $|R_a - R_d|$ is independently sampled from the vibrational ground-state wavefunction of the neutral molecule. Then the approaching distance R_a and the departing distance R_d can be adjusted accordingly. Upon photoionization, classical trajectories are launched on the cationic PES via a Franck-Condon transition, initiating time evolution[51–53]. It is acknowledged that the quasi-classical trajectory approach inherently faces the challenge of zero-point energy (ZPE) leakage during classical propagation. However, in our simulations, trajectories are predominantly sampled from the vibrational ground state of reactants, where the total initial energy is relatively low, making spurious energy flow into non-reactive modes less pronounced. Furthermore, the dimension-reduced nature of our model restricts motion to the key reactive coordinates, which indirectly reduces the phase space available for significant ZPE leakage. In the present study, we launch 10,000 reaction trajectories for each dimer system. Consistent with the RPMD analysis, we apply the identical geometric criteria ($R_a < 4$ a.u. and $R_d > 5$ a.u.) to identify the formation of H_3^+ and D_3^+[19]. The trajectories leading to the formation of H_3^+ and D_3^+ are collected to construct the yield distributions, and the reaction times are extracted using the same Gamma distribution fitting procedure as described above.

Self-consistent continuum solvation model

Using CP2K with a self-consistent continuum solvation model[40] to represent the helium solvent, we conducted molecular dynamics simulations to quantify the droplet's impact on H_3^+ and D_3^+ formation[40,54–59]. The electronic structure calculations were performed at the unrestricted PBE0/aug-cc-pVTZ level of theory. We first simulated the neutral equilibrium states of $(H_2\text{-}H_2)$ and $(D_2\text{-}D_2)$[19,20], both with and without the helium environment. These equilibrated configurations were then used as starting points, with the charge set to +1, to model the dynamical evolution of the charged complexes. For the molecular dynamics simulations incorporating the self-consistent continuum solvation model, an ensemble of 200 trajectories was propagated for each condition. To capture the complete reaction

dynamics, each trajectory was evolved for a total length of 500 fs with a timestep of 0.5 fs. The H_3^+ or D_3^+ formation was identified when the approaching distance R_a fell below 4 a.u., and the departing distance R_d exceeded 5 a.u.[19] (see Fig. 4a).

Data availability

The source data that support the main figures within this article are available from the Zenodo database[60].

Code availability

All the codes that support the findings of this study are available from the corresponding author upon request.

References

1. Ceriotti, M. et al. Nuclear quantum effects in water and aqueous systems: experiment, theory, and current challenges. *Chem. Rev.* **116**, 7529–7550 (2016).
2. Markland, T. E. & Ceriotti, M. Nuclear quantum effects enter the mainstream. *Nat. Rev. Chem.* **2**, 0109 (2018).
3. Ugur, B. E. & Webb, M. A. Nuclear quantum effects in molecular liquids across chemical space. *Nat. Commun.* **16**, 5786 (2025).
4. Balakrishnan, N. & Dalgarno, A. Chemistry at ultracold temperatures. *Chem. Phys. Lett.* **341**, 652–656 (2001).
5. Wang, T. et al. Dynamical resonances accessible only by reagent vibrational excitation in the F + HD → HF + D reaction. *Science* **342**, 1499–1502 (2013).
6. Bocus, M. et al. Nuclear quantum effects on zeolite proton hopping kinetics explored with machine learning potentials and path integral molecular dynamics. *Nat. Commun.* **14**, 1008 (2023).
7. Pérez, A., Tuckerman, M. E., Hjalmarson, H. P. & von Lilienfeld, O. A. Enol tautomers of Watson-Crick base pair models are metastable because of nuclear quantum effects. *J. Am. Chem. Soc.* **132**, 11510–11515 (2010).
8. Slocombe, L., Sacchi, M. & Al-Khalili, J. An open quantum systems approach to proton tunnelling in DNA. *Commun. Phys.* **5**, 109 (2022).
9. van de Bund, S. & Ackland, G. J. Competition between superconductivity and molecularization in the quantum nuclear behavior of lanthanum hydride. *Phys. Rev. B* **108**, 184102 (2023).
10. Balakrishnan, N. Perspective: Ultracold molecules and the dawn of cold-controlled chemistry. *J. Chem. Phys.* **145**, 150901 (2016).
11. Ospelkaus, S. et al. Quantum-state controlled chemical reactions of ultracold potassium-rubidium molecules. *Science* **327**, 853–857 (2010).
12. Hu, M.-G. et al. Direct observation of bimolecular reactions of ultracold KRb molecules. *Science* **366**, 1111–1115 (2019).
13. Liu, Y. et al. Precision test of statistical dynamics with state-to-state ultracold chemistry. *Nature* **593**, 379–384 (2021).
14. Miller, S., Tennyson, J., Geballe, T. R. & Stallard, T. Thirty years of H_3^+ astronomy. *Rev. Mod. Phys.* **92**, 035003 (2020).
15. McCall, B. J. & Oka, T. H_3^+ -an ion with many talents. *Science* **287**, 1941–1942 (2000).
16. Ekanayake, N. et al. Mechanisms and time-resolved dynamics for trihydrogen cation (H_3^+) formation from organic molecules in strong laser fields. *Sci. Rep.* **7**, 4703 (2017).
17. Ekanayake, N. et al. H2 roaming chemistry and the formation of H_3^+ from organic molecules in strong laser fields. *Nat. Commun.* **9**, 5186 (2018).
18. Alghabra, M. S. et al. Anomalous formation of trihydrogen cations from water on nanoparticles. *Nat. Commun.* **12**, 3839 (2021).
19. Zhou, L. et al. Ultrafast formation dynamics of D_3^+ from the light-driven bimolecular reaction of the D2-D2 dimer. *Nat. Chem.* **15**, 1229–1235 (2023).
20. Mi, Y. et al. D_3^+ formation through photoionization of the molecular D2-D2 dimer. *Nat. Chem.* **15**, 1224–1228 (2023).
21. Lugovoj, E., Toennies, J. P. & Vilesov, A. Manipulating and enhancing chemical reactions in helium droplets. *J. Chem. Phys.* **112**, 8217–8220 (2000).
22. Mueller, S., Krapf, S., Koslowski, T., Mudrich, M. & Stienkemeier, F. Cold reactions of alkali-metal and water clusters inside helium nanodroplets. *Phys. Rev. Lett.* **102**, 183401 (2009).
23. Farnik, M. & Toennies, J. P. Ion-molecule reactions in ^{4}He droplets: flying nano-cryo-reactors. *J. Chem. Phys.* **122**, 014307 (2005).
24. Morrison, A. M., Agarwal, J., Schaefer, H. F. & Douberly, G. E. Infrared laser spectroscopy of the CH_3OO radical formed from the reaction of CH_3 and O_2 within a helium nanodroplet. *J. Phys. Chem. A* **116**, 5299–5304 (2012).
25. Ullrich, J. et al. Recoil-ion and electron momentum spectroscopy: reaction-microscopes. *Rep. Prog. Phys.* **66**, 1463 (2003).
26. Hillenkamp, M., Keinan, S. & Even, U. Condensation limited cooling in supersonic expansions. *J. Chem. Phys.* **118**, 8699–8705 (2003).
27. Qiang, J. et al. Femtosecond rotational dynamics of D_2 molecules in superfluid helium nanodroplets. *Phys. Rev. Lett.* **128**, 243201 (2022).
28. Jochim, B., DeJesus, L. & Dantus, M. Ultrafast disruptive probing: simultaneously keeping track of tens of reaction pathways. *Rev. Sci. Instrum.* **93**, 033003 (2022).
29. Craig, I. R. & Manolopoulos, D. E. Quantum statistics and classical mechanics: real-time correlation functions from ring polymer molecular dynamics. *J. Chem. Phys.* **121**, 3368–3373 (2004).
30. De Broglie, L. Waves and quanta. *Nature* **112**, 540–540 (1923).
31. Chen, J. et al. Quantum simulation of low-temperature metallic liquid hydrogen. *Nat. Commun.* **4**, 2064 (2013).
32. Feng, Y., Chen, J., Alfè, D., Li, X.-Z. & Wang, E. Nuclear quantum effects on the high pressure melting of dense lithium. *J. Chem. Phys.* **142**, 064506 (2015).
33. You, P. et al. Quantum dynamics simulations: combining path integral nuclear dynamics and real-time TDDFT. *Electron. Struct.* **1**, 044005 (2019).
34. Fang, W., Richardson, J. O., Chen, J., Li, X.-Z. & Michaelides, A. Simultaneous deep tunneling and classical hopping for hydrogen diffusion on metals. *Phys. Rev. Lett.* **119**, 126001 (2017).
35. Feynman, R. P., Hibbs, A. R. & Styer, D. F. *Quantum Mechanics and Path Integrals Dover Books on Physics*. (Dover Publications, 2010).
36. Craig, I. R. & Manolopoulos, D. E. A refined ring polymer molecular dynamics theory of chemical reaction rates. *J. Chem. Phys.* **123**, 034102 (2005).
37. Miller, T. F. & Manolopoulos, D. E. Quantum diffusion in liquid water from ring polymer molecular dynamics. *J. Chem. Phys.* **123**, 154504 (2005).
38. Craig, I. R. & Manolopoulos, D. E. Chemical reaction rates from ring polymer molecular dynamics. *J. Chem. Phys.* **122**, 084106 (2005).
39. Ye, Z. et al. Localization and delocalization of a single molecule in a helium nanodroplet. *Phys. Rev. Lett.* **135**, 213202 (2025).
40. Andreussi, O., Dabo, I. & Marzari, N. Revised self-consistent continuum solvation in electronic-structure calculations. *J. Chem. Phys.* **136**, 064102 (2012).
41. Toennies, J. P. & Vilesov, A. F. Superfluid helium droplets: a uniquely cold nanomatrix for molecules and molecular complexes. *Angew. Chem. Int. Ed.* **43**, 2622–2648 (2004).
42. Alnaser, A. S. et al. Laser-peak-intensity calibration using recoil-ion momentum imaging. *Phys. Rev. A* **70**, 023413 (2004).
43. Chandler, D. & Wolynes, P. G. Exploiting the isomorphism between quantum theory and classical statistical mechanics of polyatomic fluids. *J. Chem. Phys.* **74**, 4078–4095 (1981).
44. Litman, Y. et al. i-pi 3.0: a flexible and efficient framework for advanced atomistic simulations. *J. Chem. Phys.* **161**, 062504 (2024).
45. Liu, Y. et al. New full-dimensional reactive potential energy surface for the H_4 system. *J. Chem. Theory Comput.* **20**, 1829–1837 (2024).
46. Sanz-Sanz, C., Roncero, O., Paniagua, M. & Aguado, A. Full-dimensional potential energy surface for the ground state of H_4^+

system based on triatomic-in-molecules formalism. *J. Chem. Phys.* **139** (2013).
47. Sanz-Sanz, C., Aguado, A., Roncero, O. & Naumkin, F. Non-adiabatic couplings and dynamics in proton transfer reactions of H_n^+ systems: application to $H_2 + H_2^+ \rightarrow H + H_3^+$ collisions. *J. Chem. Phys.* **143** (2015).
48. Kapil, V., Behler, J. & Ceriotti, M. High order path integrals made easy. *J. Chem. Phys.* **145**, 234103 (2016).
49. Hirshberg, B., Rizzi, V. & Parrinello, M. Path integral molecular dynamics for bosons. *Proc. Natl. Acad. Sci.* **116**, 21445–21449 (2019).
50. Hirshberg, B., Invernizzi, M. & Parrinello, M. Path integral molecular dynamics for fermions: Alleviating the sign problem with the Bogoliubov inequality. *J. Chem. Phys.* **152**, 171102 (2020).
51. Shi, M. et al. Impact of nuclear motion on light-induced bimolecular interaction dynamics. *Phys. Rev. X* **14**, 041001 (2024).
52. Huang, H., Hou, H., Wen, J., Ni, H. & Wu, J. Ultrafast formation dynamics of D_3^+ from bimolecular reaction of the D_2 – D_2 dimer. *Phys. Rev. A* **109**, 043107 (2024).
53. Jiang, Z. et al. Ultrafast photoinduced C-H bond formation from two small inorganic molecules. *Nat. Commun.* **15**, 2854 (2024).
54. Kühne, T. D. et al. CP2K: an electronic structure and molecular dynamics software package - Quickstep: Efficient and accurate electronic structure calculations. *J. Chem. Phys.* **152**, 194103 (2020).
55. Yin, W.-J., Krack, M., Li, X., Chen, L.-Z. & Liu, L.-M. Periodic continuum solvation model integrated with first-principles calculations for solid surfaces. *Prog. Nat. Sci.: Mater. Int.* **27**, 283–288 (2017).
56. Hutter, J., Iannuzzi, M., Schiffmann, F. & VandeVondele, J. CP2K: atomistic simulations of condensed matter systems. *Wiley Interdiscip. Rev.: Comput. Mol. Sci.* **4**, 15–25 (2014).
57. Guidon, M., Schiffmann, F., Hutter, J. & VandeVondele, J. Ab initio molecular dynamics using hybrid density functionals. *J. Chem. Phys.* **128**, 214104 (2008).
58. Kolafa, J. Time-reversible always stable predictor-corrector method for molecular dynamics of polarizable molecules. *J. Comput. Chem.* **25**, 335–342 (2004).
59. Nosé, S. A molecular dynamics method for simulations in the canonical ensemble. *Mol. Phys.* **100**, 191–198 (2002).
60. Chen, J. et al. Ultrafast bimolecular reaction catalysis via engineered nuclear quantum effects in helium nanodroplets [Data set]. *Zenodo* https://doi.org/10.5281/zenodo.20441543 (2026).

Author contributions

J.W. coordinated this project. W.Z. conceived and designed the study. J.C., Z.Y., Y.H., M.S., X.L.L, W.Z., and J.W. contributed to the experimental measurements and data analysis, L.Z., H.H., C.S.S., O.R., L.L., X.Z.L., H.N., and Z.L. contributed to the simulations. J.C., L.Z., H.H., H.N., Z.L., W.Z. and J.W. wrote the paper. All authors participated in the discussion of the results and commented on the manuscript.

Funding

This work has been supported by the Quantum Science and Technology-National Science and Technology Major Project (Grant No. 2024ZD0300700), the National Key R&D Program (Grant No. 2023YFA1406801), the National Natural Science Foundation of China (Grants No. 12304377, No. 12521003, No. 12227807, No. 12241407, No. 92250303, No. 12234002, and No. 12474341), the Science and Technology Commission of Shanghai Municipality (Grant No. 23JC1402000), and the Shanghai Pilot Program for Basic Research (Grant No. TQ20240204).

Competing interests

The authors declare no competing interests.

Additional information

Supplementary information The online version contains supplementary material available at https://doi.org/10.1038/s41467-026-76012-6.

Correspondence and requests for materials should be addressed to Hongcheng Ni, Zheng Li, Wenbin Zhang or Jian Wu.

Peer review information *Nature Communications* thanks Marcos Dantus, Andre Staudte and the other anonymous reviewer(s) for their contribution to the peer review of this work. A peer review file is available.